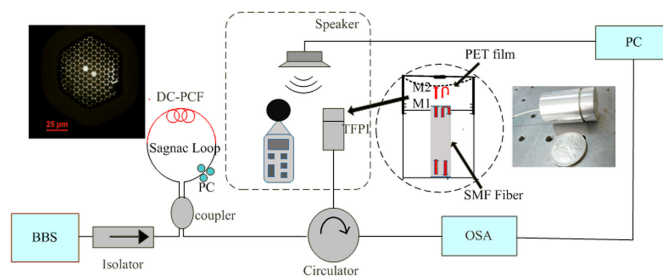# All-Optical Demodulation Fiber Acoustic Sensor With Real-Time Controllable Sensitivity Based on Optical Vernier Effect

Shuai Wang
Shun Wang
Rui-Bo Jin
Mingzhe Feng
Shun Wu
Liang Zhang
Peixiang Lu

All-Optical Demodulation Fiber Acoustic Sensor With Real-Time Controllable Sensitivity Based on Optical Vernier Effect

Shuai Wang,[1] **Shun Wang** ,[1] **Rui-Bo Jin,**[1] **Mingzhe Feng,**[1] **Shun Wu,**[1] **Liang Zhang,**[2] **and Peixiang Lu**[1,3]

[1]Hubei Key Laboratory of Optical Information and Pattern Recognition, Wuhan Institute of Technology, Wuhan 430205, China
[2]Shenzhen Institutes of Advanced Technology, Chinese Academy of Sciences, Shenzhen 518055, China
[3]School of Physics and Wuhan National Laboratory for Optoelectronics, Huazhong University of Science and Technology, Wuhan 430074, China

Abstract: In the fiber sensing research area, a pair of sharp contradictions is highlighted: high sensitivity and large dynamic range. In addition, the question of how to enable user-editable features for fiber optic sensors is gaining more and more attention. This letter presents a fiber acoustic sensor with real-time controllable sensitivity based on the optical vernier effect, which is possibly a solution to such a problem. The optical vernier structure with amplified and real-time tunable detection sensitivity is formed by cascading a Sagnac interferometer and a laboratory-made tunable Fabry–Perot interferometer (FPI). Sound pressure and frequency of the acoustic signal can be all-optically demodulated simultaneously by spectral reading and spectral scanning method, respectively. Experimental results show a real-time controllable acoustic sensitivity ($1\times$, $5\times$, and $10\times$ are demonstrated) and a maximum sensitivity is as high as 37.1 nm/Pa ($10\times$ of single FPI) within relatively large sound pressure range of 62.2–92.4 dB. By adjusting the FPI cavity length in real time, sensitivity can be controlled to meet the needs of different users or occasions. The proposed sensor has merits of controllable sensitivity in real time, high sensitivity, and large dynamic range, enabling the applications related but not limited to acoustic sensing.

Index Terms: Optical fiber acoustic sensor, controllable sensitivity, optical vernier effect.

1. Introduction

Optical fiber acoustic sensors (OFAS) have attracted considerable attention in many fields, such as structural health detection [1], seismic observation [2], leakage detection [3], and underwater positioning [4], etc. In the past years, many schemes such as fiber Bragg grating [5], long period grating [6], ultra-long period fiber grating [7], optical fiber taper [8], fiber coupler [9], MEMS [10] and DFB/DBR lasers [11], are widely used in the research of OFAS.However, the grating-type sensors require complex UV-light mask technology; Fiber tapers are often used within interference structures, which increases the complexity of the overall structure; Fiber couplers do not have flat frequency response; The manufacturing process of MEMS or DFB/DBR based acoustic sensor is

complicated. Meanwhile, some simple interference structures are also widely utilized, such as Mach-Zehnder interferometers (MZI) [12], Sagnac interferometers (SI) [13], Michelson interferometers (MI) [14], and Fabry-Perot interferometers (FPI) [15]. Interference structures like the MZI, SI, and MI have high sensitivity but have large size and they are usually suffering from cross sensitivity caused by multiple parameters such as temperature, stress, strain, and so on. Due to the small size, high sensitivity and good stability, FPI plays an important role in the field of OFAS.

In the fiber sensing research, the measurement range and sensitivity often limit each other: sensors with large measurement range often have low sensitivity [16]–[18] and high sensitivity usually accompanied by a small range [19]–[21]. The most common acoustic sensors are FPI-based sensors, which usually have a high sensitivity but limited measuring range. Improving its sensitivity often means reducing the measurement range, which is a difficult problem to be solved. In addition, in order to recover acoustic signals from OFAS, the following techniques are often applied: edge filtering method [22], phase generation carrier method (PGC) [23], dual-wavelength orthogonal method [24], and spectrum interrogation method [25]. The edge filtering method needs complicated Q-point tracking and stabilization techniques [22], [26]; the PGC method requires precise control on the external modulation signal; And strict wavelength control is necessary for the dual-wavelength orthogonal method; In contrast, the spectrum interrogation method, which demodulates the dynamic signal by extracting the ripple spectrum from the disturbed spectrum, not only avoids the shortcomings of the above methods, but also greatly eliminates environmental disturbances such as temperature and refractive index. Therefore, this method has good application prospect in the research of OFAS. Overall, an OFAS with controllable and high sensitivity with large measurement range is of great significance in the sensing research and application.

This paper presents an optical fiber acoustic sensor with real-time controllable sensitivity based on optical vernier effect. The optical vernier structure with amplified and real-time tunable detection sensitivity is formed by cascading a SI and a tunable FPI(An acoustical FP cavity with a real-time controllable cavity length). When external acoustic signal acts on the FPI sensing element, the composite film deforms and vibrates synchronously with the sound. Since the film vibration caused by the sound introduces phase modulation into the sensor [27], the acoustic signal can be detected by demodulating the phase change. Sound pressure of the acoustic signal can be measured by demodulating the spectrum drift of the optical vernier structure. And the frequency of the acoustic signal can be demodulated by demodulating the dynamic spectrum using the spectrum interrogation method [25]. The experimental results demonstrate a real-time controllable acoustic sensitivity of the sensor ($1\times$, $5\times$, $10\times$ of single FPI) and a maximum sensitivity that is as high as 37.1 nm/Pa ($10\times$ of single FPI) within a relatively large sound pressure range of 62.2–92.4 dB. By adjusting the cavity length of the FPI in real time, the system sensitivity can be controlled. What's more, highly sensitivity and large sound pressure measuring range can be obtained simultaneously, breaking the contradiction between sensitivity and measurement range. The proposed sensor offers several advantages such as controllable sensitivity in real time, high sensitivity and large dynamic range, which further benefits its practical sensing application.

2. Principle

2.1 Demodulation Principle of Sound Pressure

When an acoustic signal is applied to the sensor, the film deforms and vibrates synchronously with the sound, thereby changing the optical path difference (OPD) of the interferometer. Since the interference phase is related to the OPD, the acoustic vibration of the film introduces phase modulation into the sensor, the film deflection is proportional to the sound pressure [27]. Therefore, the acoustic signal can be detected by demodulating the phase change. When the optical spectrum analyzer (OSA) scans at high speed with low resolution, the OSA can not distinguish the high frequency vibration of the diaphragm, and the deformation of the polymer film caused by the sound pressure can be regarded as static deformation. The change of OPD will cause the peak wavelength drift of vernier spectrum. The detection sensitivity is amplified by the optical vernier structure formed
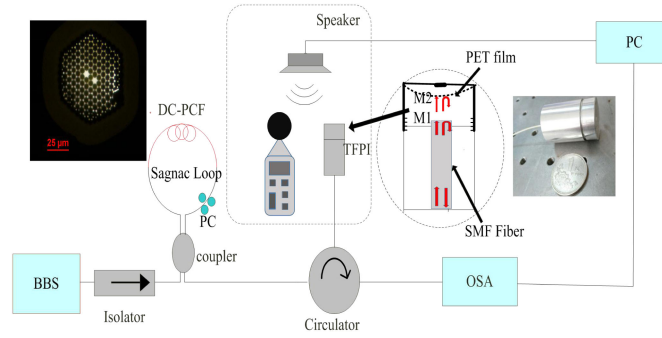
Fig. 1. Schematic diagram of experimental device. BBS, Broadband light source; DC-PCF, Dual-core photonic crystal fiber; OSA, Optical spectrum analyzer; PC, Personal computer.

by the cascaded fiber Sagnac interferometer (FSI) and FPI. The sound pressure of the acoustic signal can be measured by demodulating the spectral envelope drift of the optical vernier structure. Real-time adjustment is realized by tuning the cavity length of FPI, and different sensitivity can be selected with small effect on the measurement range.

The schematic diagram of an acoustic sensor based on tunable FPI and FSI hybrid cascade structure is shown in Fig. 1. The FSI, where there is a dual-core photonic crystal fiber (DC-PCF) whose cross-section is shown in the inset of Fig. 1, is connected to the tunable FPI via a fiber optic circulator. The optical vernier effect spectrum is generated by reasonably controlling the free spectral range (FSR) of the FPI and FSI. The transmission spectrum of FSI is approximated by the wavelength sine function, which can be described by Equation 1. From Equation 2, we can deduce the FSR between two adjacent peaks.

$$I_{FSI} = (1 - \cos(2\pi BL_1/\lambda))/2. \tag{1}$$

$$FSR_{FSI} = \lambda^2/BL_1. \tag{2}$$

B and L are the birefringence coefficient and length of the DC-PCF, respectively. In this experiment, FSI is only used as a reference interferometer, not measurement part. And the reference interferometer FSI is working as the basis of the vernier spectrum, which imposing a sinusoidal variation in the spectrum. Due to the merits of simplicity, stability and unsusceptible to external disturbances compared with MI or MZI structure, we chose FSI as our reference interferometer. The reflection spectrum function of FPI can be expressed as:

$$I_{FP} = R_1{}^2 + (1 - \alpha)^2(1 - R_1)^2 R_2{}^2$$
$$+ 2(1 - \alpha)(1 - R_1) \times R_1 R_2 \cos(4\pi nL_2/\lambda \tag{3}$$

Where α is the transmission loss of the composite film; R1 and R2 are the reflection coefficients of the fiber end face M1 and the film M2, respectively; L is the length of the FP cavity; n = 1 is the refractive index of the cavity filled with air; λ is the wavelength. Thus the FPI's FSR is

$$FSR_{FPI} = \lambda^2/2nL_2. \tag{4}$$

Phase $\phi = 4\pi nL_2/\lambda$, when the phase is $2m\pi$, the corresponding peak wavelength is

$$\lambda_m = 2nL_2/m. \tag{5}$$

Since the cavity is filled with air, external temperature disturbances to the FPI, as a sensing interferometer, can be neglected. The sound pressure will change the cavity length and lead to the drift of the peak wavelength. The drift of the peak wavelength caused by sound pressure P is shown

in the following equation.

$$\Delta\lambda\,(P) = \lambda\frac{\Delta L\,(P)}{L}. \tag{6}$$

The FPI used in this experiment is an acoustic FP cavity with controllable cavity length (tunable FPI), which is composed of thread cylinder, sleeve, thread sleeve, optical fiber, composite film and other components [15]. The cavity length can be adjusted in real-time by rotating the thread sleeve. At the front of the sensor head is a composite film consisting of a round film doped with polyethylene terephthalate and a piece of thin aluminum foil. The thin and small round aluminum foil is 3 μm in thickness and 3 mm in diameter, which will not lead to a non-negligible effect on the sensing sensitivity, but can improve the reflectivity of the film and maintain the smoothness and stability of the center vibration surface. When the vibration occurs, the deformation in different positions of the polymer film differs, while the bump made of aluminum foil will keep the two reflective surfaces parallel.

The total output spectrum of the vernier structure is the output superposition spectrum of two single interferometers. The peak appears at the wavelength where the interference peaks of FSI and FPI overlap, and the intensity of each peak is determined by the amount of the overlap. Thus, the highest peak of the total output appears at the wavelength where both interference peaks output simultaneously. All the peaks form an envelope, and the FSR of which is

$$FSR_{envelope} = \frac{FSR_{FSI} * FSR_{FPI}}{|FSR_{FPI} - FSR_{FSI}|}. \tag{7}$$

When the peak wavelength of the FPI drifts, assuming the amount of drift is $\Delta\lambda = |FSR_{FPI} - FSR_{FSI}|$, the peak of the spectrum of the vernier structure will jump to the adjacent peak. Thus the amount of drift of the envelope can be given by Equation 8, where M is the amplification factor.

$$\Delta\lambda_{envolop} = \Delta\lambda \times M = \Delta\lambda \times \frac{FSR_{FSI}}{|FSR_{FPI} - FSR_{FSI}|}. \tag{8}$$

2.2 Demodulation Principle of Acoustic Frequency

When we demodulate the frequency of the acoustic signal, the OSA is set to scan at a slow speed with high resolution so as the film deformation cannot be regarded as static but synchronized with the sound vibration when the acoustic signal acts on the sensor. The vibrating film periodically changes the cavity length of FPI over time, causing its spectrum to drift back and forth. Therefore, the intensity of the light at a fixed wavelength will fluctuate, and the spectrum under the acoustic signal is a function of wavelength and time. During the scanning process, since the light intensity of different wavelengths is monitored at different time, a dynamic spectrum changing with respect to the acoustic signal can be generated. The frequency component of the acoustic signal can be derived from the analysis of the dynamic spectrum based on the wavelength sweep speed. By implementing subtraction between the dynamic spectrum and the self-fitting curve, a ripple spectrum in time domain can be obtained. Besides, the envelope of the ripple spectrum can be removed to obtain the time domain signal of the acoustic signal [25]. It is assumed that the spectrum under the action of the acoustic wave is a dynamic spectrum $S(\lambda, t)$. The static spectrum $S(\lambda)$ acquired by averaging the upper and lower envelopes $S_1(\lambda)$ and $S_2(\lambda)$ obtained by self-fitting dynamic spectrum has the same external interference as the dynamic spectrum itself, so the ripple spectrum $\Delta S(\lambda, t)$, achieved by the subtraction operation, eliminates the influence of external interference. The ripple spectrum, expressed as Equation 10, is the difference between the dynamic spectrum and the static spectrum. Since the spectrum is obtained by scanning the light intensity at a certain speed in a certain wavelength range, the time t can represent the quotient of the wavelength difference and the scanning speed. In Equation 11, λ is the wavelength, λ_0 is the wavelength at where scanning

begins, and V (nm/s) is the scanning speed.

$$S(\lambda) = \frac{S_1(\lambda) + S_2(\lambda)}{2} \tag{9}$$

$$S(\lambda, t) = S(\lambda) + \Delta S(\lambda, t) \tag{10}$$

$$t = \frac{\lambda - \lambda_0}{V}, \Delta S(\lambda, t) = \Delta S\left(\lambda, \frac{\lambda - \lambda_0}{V}\right) \tag{11}$$

In general, the spectrum variation (wavelength or intensity) should have a linear relationship, independent of time, with the acoustic pressure [28]. Of which the time parameter can be separated from the ripple spectrum. In addition, the spatial angular frequency of the spectrum itself will have an impact on the acoustic frequency signal [29]. Therefore, for a pure tone signal with sinusoidal variation and frequency of ω, its ripple spectrum can be expressed as

$$\Delta S(\lambda, t) = \Delta S\left(\lambda, \frac{\lambda_1 - \lambda_0}{V}\right)_{rise} + \Delta S\left(\lambda, \frac{\lambda_2 - \lambda_0}{V}\right)_{decline}$$

$$= \Delta S(\lambda)\cos\left[(\omega + \beta)\frac{\lambda_1 - \lambda_0}{V}\right] + \Delta S(\lambda)\cos\left[(\omega - \beta)\frac{\lambda_2 - \lambda_0}{V}\right] \tag{12}$$

Here β is the spatial angular frequency, λ_1 and λ_2 are the wavelength at the rising edge and falling edge respectively, and $\Delta S(\lambda)$ are the amplitude of the wavy spectrum.

$$\Delta S(\lambda) = \frac{S_1(\lambda) - S_2(\lambda)}{2} \tag{13}$$

Therefore, the ripple spectrum after removal of the envelope can be obtained by the following formula 14. At high frequencies, the spatial angular frequency is negligible relative to the frequency of the acoustic signal. The acoustic signal in time domain can be approximated as the ripple spectrum after the envelope is removed.

$$\cos(\omega t) = \cos\left(\omega\frac{\lambda - \lambda_0}{V}\right) \approx \cos\left[(\omega + \beta)\frac{\lambda_1 - \lambda_0}{V}\right]$$

$$+ \cos\left[(\omega - \beta)\frac{\lambda_2 + \lambda_0}{V}\right] = \frac{S(\lambda, t) - S(\lambda)}{\Delta S(\lambda)}$$

$$= \frac{2(S(\lambda, t) - S(\lambda))}{S_1(\lambda) - S_2(\lambda)}. \tag{14}$$

In the above formula, ω is the frequency of the demodulated acoustic signal, and β is the spatial angular frequency. By performing a fast Fourier transform, two peaks with frequencies of $\omega + \beta$ and $\omega - \beta$ can be obtained. From the previous analysis, the frequency of the acoustic signal is the mean value of the two frequency components.

3. Simulation

3.1 Simulation of Optical Vernier Effect

The simulation results of optical vernier effect are shown in Fig. 2. FSR_{FSI} is set to 3.02 nm, FSR_{FPI} is set to 2.67 nm, and $FSR_{envelope}$ is calculated as 23 nm. Figure 2 indicates that the 3.02 nm shift of the envelope respects to the 0.35 nm peak wavelength shift of the interference fringe in FPI, achieving an 8.6 times amplification on the sensitivity, which is consistent with the previous analysis.

3.2 Demodulation Simulation of Sound Signal Frequency

In the demodulation simulation of the acoustic signal frequency, the acoustic signal frequency and the scanning speed of the optical spectrum analyzer are 50 Hz and 4 nm/s, respectively, with
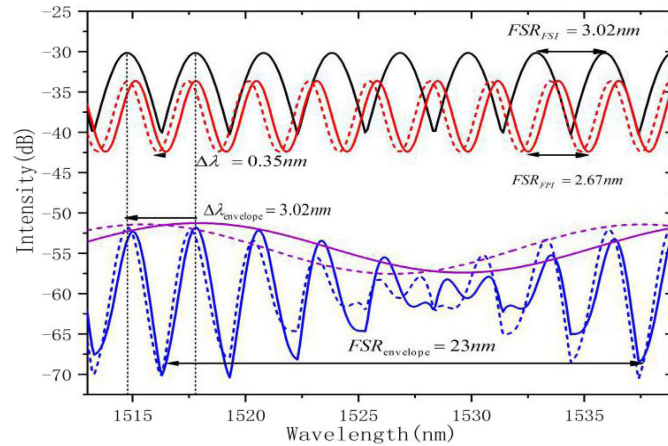
Fig. 2. The simulation result of Vernier-effect. The black line is the interference spectrum of FSI. The red solid line and the red dotted line are the interference spectra of FPI before and after the shift of peak wavelength respectively. The solid blue line and dotted blue line show the output spectrum of the vernier structure before and after the shift of the peak wavelength respectively. The purple solid line and the purple dotted line are respectively the envelope of the output spectrum of the vernier structure before and after the shift of the peak wavelength.
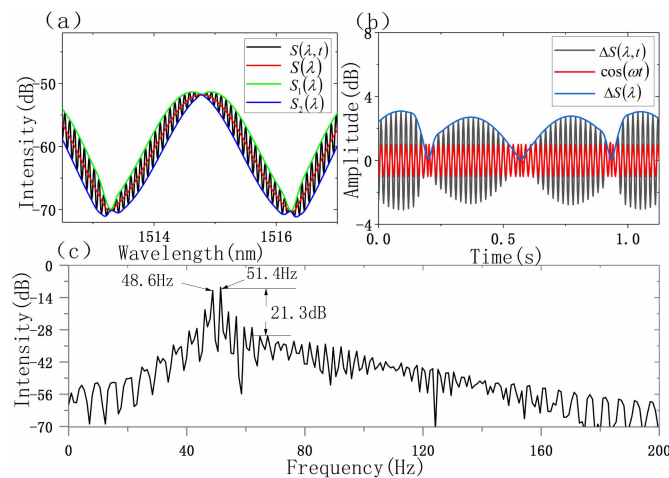

Fig. 3. Simulation demodulation results of the acoustic frequency when acoustic signal is disturbed at 50 Hz. (a) Dynamic spectrum, its upper and lower envelope, and a self-fitting static spectrum. (b) The ripple spectrum, its envelope curve and the extracted acoustic signal. (c) Fast Fourier transform of the extracted sound signal.

the scanning wavelength range from 1512.5 nm to 1517 nm. The simulated spectrum is shown in Fig. 3(a). As shown, the dynamic spectrum, its upper and lower envelopes, the fitted static spectrum are represented by black, green, blue, and red lines, respectively. The black line in Fig. 3(b) shows the ripple spectrum, and the blue line represents the difference between the upper and lower envelopes. According to the above analysis, we can use Equation (14) to eliminate the envelope, and it can be considered as an extracted acoustic signal that is shown by the red line. The frequency of the rising and falling edges is slightly different due to the influence of the spatial angular frequency, causing a slight change in its period. At the intersection of the rising and falling edges (dips in blue line), the period changes, which causes confusion. Fig. 3(c) shows the fast Fourier transform (FFT) processing results of the extracted sound signal wave. It can be seen that two peaks at 48.6 Hz and 51.4 Hz emerge in the frequency domain, which are the frequency of the ripple spectrum at the falling edge and the rising edge, respectively. Their mean value 50 Hz implies the acoustic signal
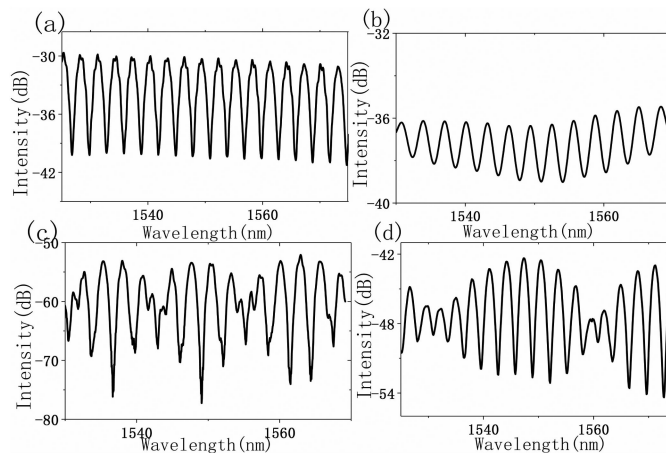
Fig. 4. Output spectrum of a single interferometer and output spectrum under a cascade structure. (a) Single FSI output spectrum. (b) Single FPI output spectrum. (c) The output spectrum of the optical vernier structure after adjusting the cavity length of the FPI to 0.476 mm. (d) The output spectrum of the optical vernier structure by adjusting the cavity length of the FPI to 0.418 mm.

to be measured. That is consistent with the previous analysis and the feasibility of this approach is well demonstrated.

4. Experiments

4.1 The Experiment of Sound Pressure Demodulation

As shown in Fig. 1, a broadband source (BBS) is used as the input source in the experiment. The vernier structure consists of a FSI and an acoustical FP cavity with a real-time controllable cavity length. The DC-PCF has a length of 52 cm and a birefringence of 1.48×10^{-3}. The fiber end face and the polymer film attached to the outer end of the spiral sleeve form a FPI with a cavity length of 0.355 mm, and the cavity length can be adjusted by rotating the spiral sleeve. Light, passing through the FSI, is reflected by the FP cavity, and finally received by an OSA with a resolution of 0.1 nm at a scanning speed of 64 nm/s. Figure 4(a) shows the interference spectrum of a single FSI; Fig. 4(b) shows the FPI spectrum with a cavity length of 0.355 mm; and Fig. 4(c) shows the spectrum of the vernier structure with a FPI cavity length adjusted to 0.476 mm, FSR_{FPI} is 2.36 nm and $FSR_{envelope}$ is 12.1 nm. So the calculated magnification M is about 5.1; Fig. 4(d) is the spectrum of the vernier structure after a real-time adjustment with the cavity length 0.418 mm, then FSR_{FPI} is 2.69 nm, $FSR_{envelope}$ is 28 nm, and the calculated magnification M is about 10.4; In addition, as we know that the measurement range of the phase-modulated type sensor is determined by FSR. It can be seen from equation 6 that the measured sound pressure range of single FPI sensor is inversely proportional to the cavity length of the FPI. The measured sound pressure range of optical vernier structure is increases, from 12.1 nm to 28 nmalong along with the $FSR_{FPI,}$ from 2.36 nm to 2.69 nm.

To demodulate the external acoustic signal, here we keep the acoustic frequency at 200 Hz. When acoustic signal acts on the sensor, the peak wavelength of the spectrum drifts. For the vernier structure, the envelope of the spectrum also drifts. Fig. 5(a) shows the output spectrum of the FPI with cavity length of 0.335 mm under different sound pressure levels, and Fig. 5(b) is the envelope line group of the output spectrum when the FPI cavity length is adjusted to 0.476 mm under different sound pressure levels. Fig. 5(c) is an envelope line group of the output spectrum of the vernier structure under different sound pressure levels when the cavity length is adjusted to 0.418 mm. It can be seen that the drifting amount of the spectrum is different under almost the same sound pressure change. Figure 5(d) is a schematic diagram of the wavelength-sound pressure relationship. When the optical vernier effect is applied, the FPI cavity length can be adjusted in
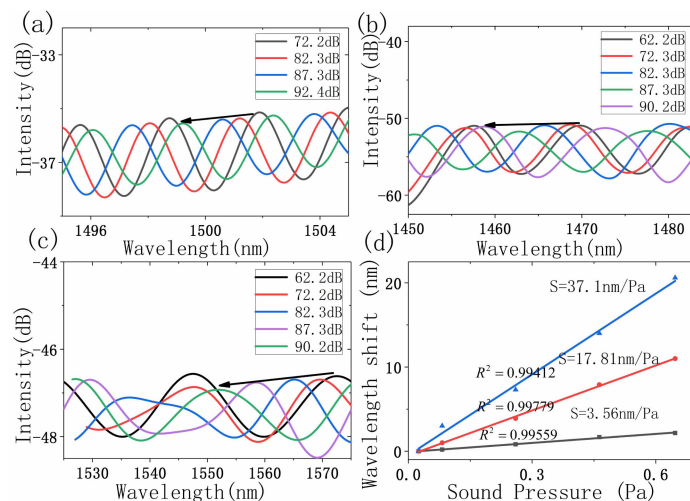
Fig. 5. The sound pressure response results of FPI with different cavity lengths with adjustment in real time. Fig. 5(a) shows the output spectrum of the FPI with cavity length of 0.335 mm under different sound pressure levels, and Fig. 5(b) shows the envelope group of the output spectrum when the FPI cavity length is adjusted to 0.476 mm under different sound pressure levels. Fig. 5(c) is an envelope group of the output spectrum of the optical vernier structure at different sound pressure levels when the cavity length is adjusted to 0.418 mm. Figure 5(d) is a plot of wavelength versus sound pressure for different magnification factors.

real-time to 0.476 mm and 0.418 mm. Compared with the single FPI sensor with a cavity length of 0.355 mm, the sensitivity of the vernier structure is increased by 5.1 times and 10.4 times, respectively. In addition, when the amplification factors are 5.1 times and 10.4 times, the measurement range are 62.6–91.1 dB and 62.2–92.04 dB, correspondingly. That means, the measurement range maintain almost unchanged with the sensitivity increases. The results imply that the contradiction between high sensitivity and large dynamic range is broken. We demonstrated an OFAS that combines the merits of high sensitivity and large dynamic range simultaneously.

As we know, the vernier structure can boost sensitivity, but it also produce a discontinuous nonlinear output. Because the readout value jumps when the spectrum shift beyond a ΔFSR range (that is FSR_{FPI}-FSR_{FSI}). Although the overall linear fitting is perfect, the vernier sensing in a very small range is hard to distinguished. This will limit our sensing resolution, the resolutions of $\times$5.1 and $\times$10.4 vernier sensors would be 0.037Pa and 0.0089Pa, respectively.

4.2 The Experiment of Demodulating the Sound Frequency

When demodulating the frequency of the acoustic signal, the fine spectrum is the processing object. Since the intensity of the wavelength at the dip is small, to avoid the influence of the noise floor, we select the band near the peak wavelength within a wavelength range of 1524–1526 nm. The parameters of the OSA here are as follows: the resolution is 0.02 nm, the sampling interval is 0.004 nm, the average time is 0.5 s, and the corresponding scanning speed is 4 nm/s. Fig. 6(a), (b) and (c) are spectra under the action of acoustic signal at frequencies 100 Hz, 200 Hz, and 800 Hz, respectively. Fig. 7(a) (b) (c) are the demodulated acoustic signals in the time domain at corresponding frequencies. At the peak wavelength, where the rising and falling edges meet, the rising edge frequency and the falling edge frequency are mixed and superimposed. So a frequency difference is produced, causing the waveform more dense here.

Fig. 8(a) (b) (c) are FFT curves of the acoustic signals implying the corresponding frequencies. The spatial angular frequency can not be ignored at low frequencies, so there will be two split peaks with little frequency difference in the frequency domain. The acoustic signal frequency to be demodulated can be the average value of the two split peaks. When the acoustic signal is at high
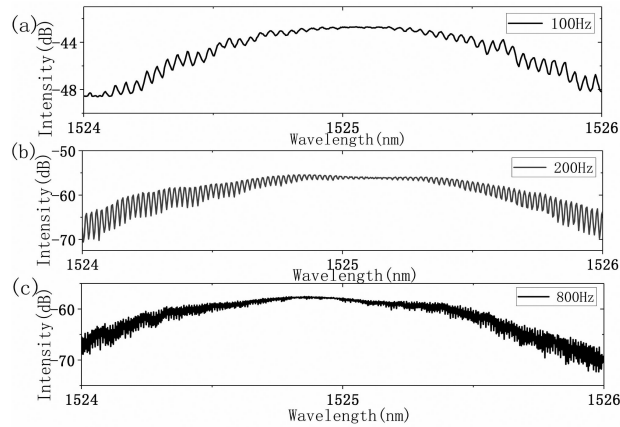
Fig. 6. Spectrum at different frequencies. (a), (b), and (c) are the spectra under action of sound signals at frequencies of 100 Hz, 200 Hz, and 800 Hz respectively.
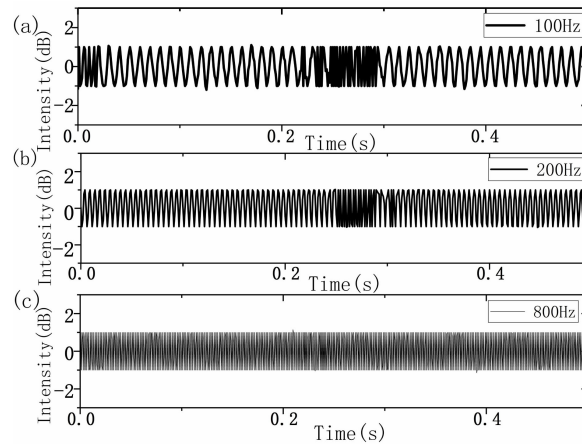

Fig. 7. Demodulated sound signals at different frequencies. (a), (b), and (c) are demodulated sound signals in time domain at 100 Hz, 200 Hz, and 800 Hz respectively.
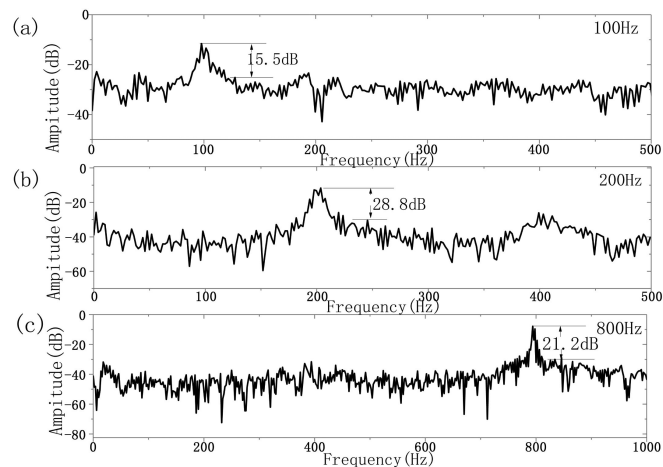

Fig. 8. The results of the demodulated sound signals in frequency domain. (a),(b), and (c) is FFT results of the demodulated acoustic signal in frequency domain.

frequency, the angular frequency of the spatial signal is negligible compared to the acoustic signal. So it can be considered that the two peaks are combined, and the acoustic signal frequency is the frequency at the peak point. In addition, other harmonic components appear in the frequency domain [25], which can be neglected in our analysis. These results are consistent with the above principle analysis, which also verifies the feasibility of the proposed scheme.

5. Conclusion

In this paper, an OFAS based on the optical vernier effect with real-time controllable sensitivity is proposed. The optical vernier effect structure is formed by cascading SI and tunable FPI. This sensor can adjust the sensitivity amplification factor in real time without negatively affecting the measurement range. The spectral interrogation method can be used to demodulate the external acoustic signal. The experimental results show a controllable sensitivity ($1\times$, $5\times$, $10\times$ of single FPI sensor) and a maximum sensitivity is as high as 37.1 nm/Pa ($10\times$ of single FPI) within relatively large sound pressure range 62.2–92.4 dB. By adjusting the FPI cavity length in real time, the sensitivity and measurement range can be further improved. The solution in this paper breaks a contradiction that high sensitivity and large dynamic range are difficult to achieve at the same time, and the performance parameters can be adjusted in real time to meet the requirements of different users or occasions.

References

[1] C. Hu, Z. Yu, and A. Wang, "An all fiber-optic multi-parameter structure health monitoring system," *Opt. Exp.*, vol. 24, no. 18, pp. 20287–20296, 2016.
[2] T. Parker *et al.*, "High definition seismic and microseismic data acquisition using distributed and engineered fiber optic acoustic sensors," in *Proc. Amer. Geophys. Union, Fall Meeting*, 2017.
[3] L. Hang, C. He, and B. Wu, "Novel distributed optical fiber acoustic sensor array for leak detection," *Opt. Eng.*, vol. 47, no. 5, pp. 525–534, 2008.
[4] S. Wang *et al.*, "Flexible piezoelectric fibers for acoustic sensing and positioning," *Adv. Electron. Mater.*, vol. 3, no. 3, 2017, Art. no. 1600449.
[5] S. Wang *et al.*, "Intensity demodulation-based acoustic sensor using dual fiber Bragg gratings and a titanium film," *J. Mod. Opt.*, vol. 61, no. 12, pp. 1033–1038, 2014.
[6] J. O. Gaudron *et al.*, "Long period grating-based optical fibre sensor for the underwater detection of acoustic waves," *Sensors Actuators A, Phys.*, vol. 201, pp. 289–293, 2013.
[7] W. Ni *et al.*, "Highly sensitive optical fiber curvature and acoustic sensor based on thin core ultra long period fiber grating," *IEEE Photon. J.*, vol. 9, no. 2, Apr. 2017, Art. no. 7100909.
[8] B. Xu *et al.*, "Acoustic vibration sensor based on nonadiabatic tapered fibers," *Opt. Lett.*, vol. 37, no. 22, pp. 4768–4770, 2012.
[9] S. Wang *et al.*, "Optical fiber acoustic sensor based on nonstandard fused coupler and aluminum foil," *IEEE Sensors J.*, vol. 14, no. 7, pp. 2293–2298, Jul. 2014.
[10] B. Liu *et al.*, "MEMS-based high-sensitivity Fabry–Perot acoustic sensor with a 45° angled fiber," *IEEE Photon. Technol. Lett.*, vol. 28, no. 5, pp. 581–584, Mar. 2016.
[11] S. W. Løvseth *et al.*, "Fiber distributed-feedback lasers used as acoustic sensors in air," *Appl. Opt.*, vol. 38, no. 22, pp. 4821–4830, 1999.
[12] D. Pawar *et al.*, "Mach–Zehnder interferometric photonic crystal fiber for low acoustic frequency detections," *Appl. Phy. Lett.*, vol. 108, no. 4, 2016, Art. no. 041912.
[13] A. Yap, T. Vo, and H. Wijaya, "Fiber optic acoustic sensor based on the Sagnac interferometer," *Proc. SPIE*, vol. 2574, pp. 87–88, 1995.
[14] L. Liu *et al.*, "Fiber-optic michelson interferometric acoustic sensor based on a PP/PET diaphragm," *IEEE Sensors J.*, vol. 16, no. 9, pp. 3054–3058, May 2016.
[15] S. Wang *et al.*, "An infrasound sensor based on extrinsic fiber-optic Fabry–Perot interferometer structure," *IEEE Photon. Technol. Lett.*, vol. 28, no. 11, pp. 1264–1267, Jun. 2016.
[16] K. S. Park, H. Y. Choi, S. J. Park, U. C. Paek, and B. H. Lee, "Temperature robust refractive index sensor based on a photonic crystal fiber interferometer," *IEEE Sensors J.*, vol. 10, no. 6, pp. 1147–1148, Jun. 2010.
[17] Y. Yang, X. Zhang, W. Jin, W. Duan, and M. Yang, "Embedded pressure sensor based on birefringent photonic crystal fiber," in *Proc. OFS 22nd Int. Conf. Opt. Fiber Sensors*, 2012, vol. 8421, Paper 842132.
[18] H. Yu, Y. Wang, J. Ma, Z. Zheng, Z. Luo, and Y. Zheng, "Fabry–Perot interferometric high-temperature sensing up to 1200 °C based on a silica glass photonic crystal fiber," *Sensors*, vol. 18, no. 1, pp. 273–281, 2018.
[19] H. Luo *et al.*, "Refractive index sensitivity characteristics near the dispersion turning point of the multimode microfiber-based Mach–Zehnder interferometer," *Opt. Lett.*, vol. 40, no. 21, pp. 5042–5045, 2015.
[20] F. Xu *et al.*, "High-sensitivity Fabry–Perot interferometric pressure sensor based on a nano thick silver diaphragm," *Opt. Lett.*, vol. 37, no. 2, pp. 133–135, 2012.

[21] M. Llera *et al.*, "Liquid-air based Fabry–Pérot cavity on fiber tip sensor," *Opt. Exp.*, vol. 24, no. 8, pp. 8054–8065, 2016.

[22] Z. Gong *et al.*, "High-sensitivity Fabry–Perot interferometric acoustic sensor for low-frequency acoustic pressure detections," *J. Lightw. Technol.*, vol. 35, no. 24, pp. 5276–5279, Dec. 2017.

[23] B. Liu *et al.*, "Diaphragm based long cavity Fabry–Perot fiber acoustic sensor using phase generated carrier," *Opt. Commun.*, vol. 382, pp. 514–518, 2017.

[24] H. Liao *et al.*, "Phase demodulation of short-cavity Fabry–Perot interferometric acoustic sensors with two wavelengths," *IEEE Photon. J.*, vol. 9, no. 2, Apr. 2017, Art. no. 7102207.

[25] X. Fu *et al.*, "Spectrum interrogation of fiber acoustic sensor based on self-fitting and differential method," *Opt. Exp.*, vol. 25, no. 4, pp. 4429–4437, 2017.

[26] F. Wang, Z. Shao, J. Xie, Z. Hu, H. Luo, and Y. Hu, "Extrinsic Fabry–Perot underwater acoustic sensor based on micromachined center-embossed diaphragm," *J. Lightw. Technol.*, vol. 32, no. 23, pp. 4026–4034, Dec. 2014.

[27] X. Fu *et al.*, "Phase interrogation of diaphragm-based optical fiber acoustic sensor assisted by wavelength-scanned spectral coding," *IEEE Photon. J.*, vol. 10, no. 3, Jun. 2018, Art. no. 7102811.

[28] F. Xu *et al.*, "Fiber-optic acoustic pressure sensor based on large-area nanolayer silver diaghragm," *Opt. Lett.*, vol. 39, no. 10, pp. 2838–2840, 2014.

[29] X. Fu *et al.*, "Analysis on fourier characteristics of wavelength-scanned optical spectrum of low-finesse Fabry–Pérot acoustic sensor," *Opt. Exp.*, vol. 26, no. 17, pp. 22064–22074, 2018.